Shear-driven swimming in laminar flow inspired by tank treading

Qiang Zhu [1,*] and Qing Xiao [2]

[1] *Department of Structural Engineering, University of California San Diego, La Jolla, California 92093-0085, USA*

[2] *Department of Naval Architecture, Ocean and Marine Engineering, University of Strathclyde, Glasgow, G4 0LZ, Scotland, United Kingdom*

(Received 16 December 2024; accepted 16 April 2025; published 1 May 2025)

To study the feasibility of shear-stress-driven locomotion in the Reynolds number range of $O(10–10^2)$, we propose an aquatic swimming system characterized by an elongated barrel-shaped body with both ends open. The side wall of the body is enwraped within a flexible membrane, which circulates around the body similar to the tank treading motion of vesicles or erythrocytes (red blood cells). During the circulation, the membrane on the outer side of the barrel and the one on the inner side travel at opposite directions (one downstream and the other upstream), generating a net thrust force due to the inner-side versus outer-side asymmetry of the design. The performance of this system has been investigated numerically by using an immersed-boundary model. The results show that this device is able to achieve forward speeds that are comparable to the circulation speed of the membrane. Further study indicates that within the targeted Reynolds number range, when the membrane circulation speed is given the swimming speed is not sensitive to the Reynolds number, although it does depend on the diameter-to-length ratio of the body.

DOI: 10.1103/PhysRevFluids.10.054101

I. INTRODUCTION

Unlike conventional underwater propulsion technology, which relies on rotational blades, biomimetic propellers utilize undulating or flapping motions of deformable bodies or body appendages (e.g., flapping fins) for force generation. The inspiration comes from the locomotion methods of aquatic verterbrates such as fish and marine mammals, or inverterbrates such as cephalopods [1–5]. These bio-inspired designs are expected to inherit useful features from their natural counterparts, including high swimming speed, high manuverability, high efficiency, and low environmental footprint.

The force needed for swimming is achieved via momentum exchange between the object and its surrounding flow field. This momentum exchange occurs in both tangential and normal directions at the fluid-solid interface, leading to normal stress and shear stress on the body. In most existing designs, the "useful" part of the fluid-body interaction force, i.e., the thrust force that aligns with the intended swimming direction, comes primary from the normal stress, even though this stress also contributes to the generation of form drag. In contrast, the shear stress contributes mostly to drag production in the form of skin friction.

However, shear stress plays pivotal roles in fluid-structure interactions in viscosity-dominated flows. One example is the tank-treading responses of vesicles or erythrocytes in viscous shear flow [6–9]. Structurally, these microscopic entities are essentially droplets of liquid enwraped within highly flexible membranes made of lipid and proteins. In a shear flow, the membrane of such a

*Contact author: qizhu@ucsd.edu

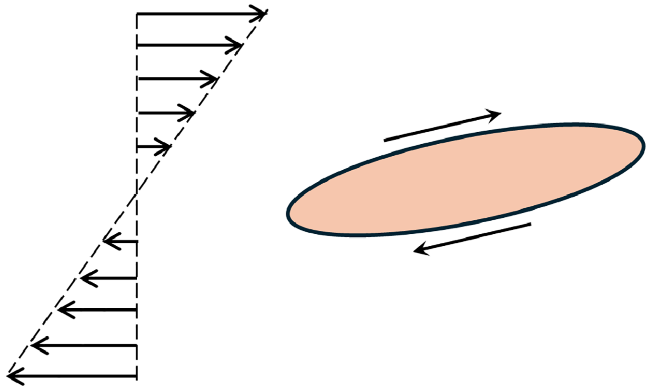

FIG. 1. Tank-treading response of microscopic vesicles or cells in shear flow.

biological structure circulates around its body driven by the shear stress exerted on the surface, which is reminiscent of the continuous track of a tracked vehicle (Fig. 1). It has been pointed out that by locally varying the bending stiffness of the membrane of such an object, it is possible to achieve controlled passive swimming in a shear flow via tank treading [10].

Tank treading may also provide a means of active swimming without the help of external flow field. For instance, Purcell described a "toroidal swimmer," a hypothetical creature that propels itself via tank-treading motion of its membrane [11]. As shown in Fig. 2, the body of this creature has a shape of a ring torus. Its membrane circulates in the poloidal direction [see Fig. 2(b)] to generate thrust. The feasibility of this design has been demonstrated through theoretical and numerical analyses [12,13]. Recently, a toroidal robot has been developed [14]. Made of liquid crystal elastomer, this donut-shaped system is able to absorb energy from light and swim in Stokes regime where the Reynolds number is much smaller than one.

The aforementioned studies about the passive or active tank treading motions and their applications in locomotion are all conducted in Stokes flows, where the inertia effect is negligibly small. These locomotion strategies, however, are not used by any existing systems in nature. To date there is no artificial systems in application based on these designs either. The difficulty lies in

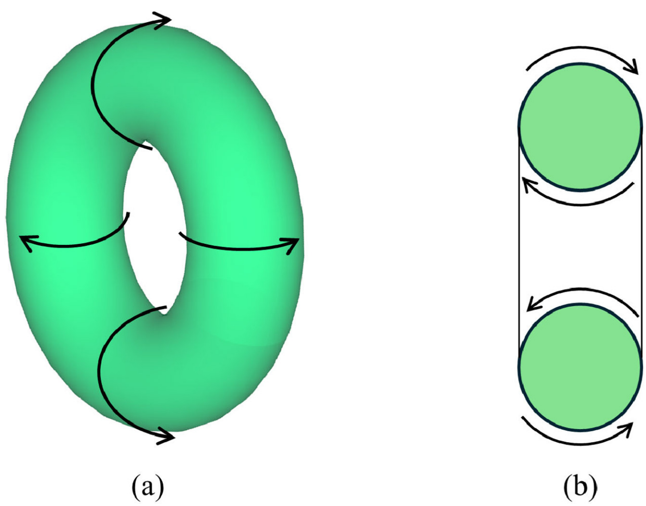

FIG. 2. (a) Three-dimensional view and (b) cross-sectional view of the toroidal swimmer [11].

the creation of artificial swimmers with sophisticated activation devices to achieve the required membrane circulation or stiffness change that are sufficiently small to reach the low Reynolds number regime. For perspective, the size of a red blood cell is around 8 μm, which is hard to be duplicated in manmade systems with today's technology. Alternatively, without shrinking the length scale of the swimmer, a high-viscosity material (polydimethylsiloxane, or PDMS) was used as the surrounding fluid to achieve Stokes flow condition [14]. This will severely restrict the potential application of the technology.

There do exist a few numerical simulations of the toroidal swimmer at finite Reynolds numbers [15,16]. According to these studies, depending on the Reynolds number and the aspect ratio of the swimmer, there are two swimming modes with opposite swimming directions, the shear-driven mode and the jet-driven mode. A similar conclusion was reached in a two-dimensional examination of the swimming performance of a pair of counterrotating cylinders [17]. The shear-driven mode occurs when the Reynolds number and/or the aspect ratio are low. In this mode the shear stress provides the propulsion force in the swimming direction, whereas the pressure thwarts the forward motion. Due to the blunt geometry of the object, the pressure effect and the form drag it brings are large, which affects the swimming performance of the system. Moreover, the energetics of the problem has not been studied.

It is the purpose of this work to explore the feasibility of high effective swimming by applying the shear-driven propulsion mode. Toward this end we will use a body geometry which suppresses form drag while enhances shear stress parallel to the swimming direction. The performance of this system is studied in the range of Reynolds number around $O(10\text{–}10^2)$. Physically, this is the Reynolds number of artificial aquatic swimmers in the millimeter to centimeter range of length scale, which might be within the reach in the near future.

Toward this end, a fluid-structure interaction model based on the immersed-boundary framework has been developed to simulate the propulsion performance in both tethered and free-swimming scenarios of a swimmer whose membrane circulates around its body in a tank-treading style. The thrust generation capacity, free-swimming speed, and energy expenditure during the process will be investigated.

The rest of the paper is organized as follows. Section II contains a depiction of the physical system to be studied, including its geometry and the kinematics of the membrane circulation for thrust generation. This is followed in Sec. III by a brief description of the mathematical formulation and the numerical algorithm. The numerical results are then presented in Sec. IV. Finally, in Sec. V, conclusions are drawn.

II. PHYSICAL PROBLEM

Unlike Purcell's toroidal swimmer shown in Fig. 2, we choose an elongated body shape with decreased projected area in the direction of swimming to reduce form drag and increased area of the side surface for more effective momentum exchange between the body and the fluid via shear stress. As shown in Fig. 3, we consider a barrel-shaped body consisting of a wall around a cylindrical empty chamber which is open in both ends. The diameter of the body is D. The axis of symmetry of the body coincides with the x axis. The radial axis is r. The wall of the barrel is made of a deformable zero-thickness membrane enwraping fluid inside. The thickness of the wall is d. For simplicity, it is assumed that the fluid wrapped within the membrane (i.e., the interior fluid) has the same physical properties, hereby density ρ and dynamic viscosity μ, as the exterior fluid. The cross-sectional view of the wall within the x-r plane is shown in Fig. 3(b). Its thickness is d, and its length is L (not counting for the semicircles on the ends).

Driven by an activation system that is not included in the model, the membrane circulates around the body in a manner shown in Fig. 3. During the circulation, the membrane on the inner side of the wall moves in the $-x$ direction, whereas the one on the outer side of the wall moves in the x direction. The speed of the membrane motion is V. Meanwhile, the geometry of the wall and its surface area remain unchanged. Since the intended swimming direction is $-x$, hereafter the flow

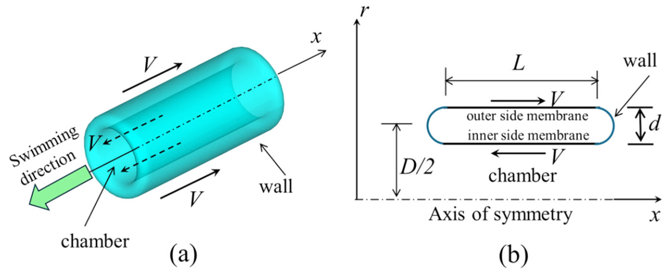

FIG. 3. (a) The three-dimensional view and (b) the cross-sectional view within the x-r plane of the physical problem.

to the left side of the swimmer is called the upstream flow and the one to the right side is called the downstream flow. Correspondingly, the leftmost point on the wall is the leading edge and the rightmost point is the trailing edge.

The dynamics of the system is determined by three independent dimensionless parameters, the aspect ratio (diameter-to-length ratio) of the body D/L, the thickness-to-length ratio of the wall d/L, and the Reynolds number $R_e \equiv \rho V L/\mu$.

III. MATHEMATICAL FORMULATIONS AND NUMERICAL APPROACH

A. Governing equations

Within the immersed-boundary framework, the fluid motion is governed by the axisymmetric Navier-Stokes equation as

$$\rho\left(\frac{\partial u_x}{\partial t} + \mathbf{u}\cdot\nabla u_x\right) + \frac{\partial p}{\partial x} - \mu\left[\frac{\partial^2 u_x}{\partial x^2} + \frac{1}{r}\frac{\partial}{\partial r}\left(r\frac{\partial u_x}{\partial r}\right)\right] - f_x = 0,$$

$$\rho\left(\frac{\partial u_r}{\partial t} + \mathbf{u}\cdot\nabla u_r\right) + \frac{\partial p}{\partial r} - \mu\left[\frac{\partial^2 u_r}{\partial x^2} + \frac{1}{r}\frac{\partial}{\partial r}\left(r\frac{\partial u_r}{\partial r}\right) - \frac{u_r}{r^2}\right] - f_r = 0,$$

$$\frac{\partial u_x}{\partial x} + \frac{1}{r}\frac{\partial (r u_r)}{\partial r} = 0, \tag{1}$$

where $\mathbf{u} \equiv (u_x, u_r)$ is the flow velocity. $\mathbf{f} \equiv (f_x, f_r)$ is the force exerted by the solid object on the fluid, which is determined via its relation with $\mathbf{F} \equiv (F_x, F_r)$, the force exerted by the fluid on the solid object. We have

$$\mathbf{f}(\mathbf{x}, t) = \int_\Gamma \mathbf{F}(s, t)\delta(\mathbf{X}(s, t) - \mathbf{x})ds, \tag{2}$$

where $\mathbf{x} \equiv (x, r)$. Γ represents the contour where the membrane is located, and s is a Lagrangian coordinate along this contour. $\mathbf{X}$ is the location of a point on the contour measured in the (x, r) coordinate system.

To enforce the no-slip and no-flux conditions at the fluid-solid interface, we use a penalty method in which neighboring fluidic and structural particles are connected with springs to keep them from drifting away from each other. Subsequently, we have

$$\mathbf{F}(s, t) = \alpha \int_0^t [\mathbf{U}(s, \tau) - \mathbf{V}(s, \tau)]d\tau + \beta[\mathbf{U}(s, t) - \mathbf{V}(s, t)], \tag{3}$$

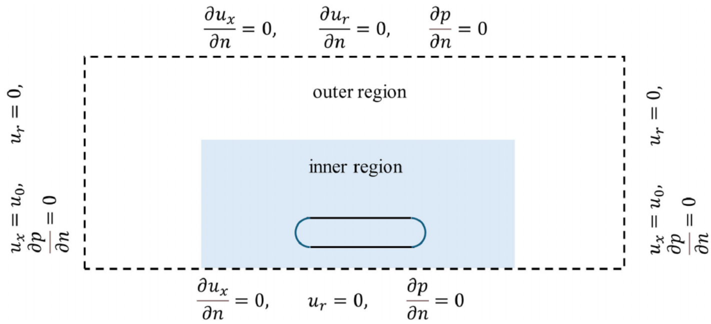

FIG. 4. The computational domain and boundary conditions.

where $\mathbf{V}$ is the structural velocity, and $\mathbf{U}$ is the fluid velocity at the fluid-structure interface obtained as

$$\mathbf{U}(s,t) = \int_{\Omega} \mathbf{u}(\mathbf{x},t)\ \delta(\mathbf{x} - \mathbf{X}(s,t))d\mathbf{x}, \tag{4}$$

where Ω is the fluid domain.

In Eq. (3), α and β are the stiffness and damping coefficient of the spring. If these numerical parameters are sufficiently large, then their values have no effect on the results.

The net force on the body F_b is defined as the hydrodynamic force on the body in the $-x$ direction, which is obtained by integrating the fluid forcing F_x over the contour of the body so that

$$F_b = -\int_{\Gamma} 2\pi r(s) F_x(s,t) ds. \tag{5}$$

The power expenditure P is obtained as

$$P = \int_{\Gamma} 2\pi r \mathbf{F} \cdot \mathbf{U} ds. \tag{6}$$

The forward motion (hereby the body displacement of the center of the mass in the $-x$ direction) x_b is determined through Newton's law as

$$m_b \frac{d^2 x_b}{dt^2} = F_b, \tag{7}$$

where m_b is the mass of the swimming body.

B. Numerical method

The problem formulated in Sec. III A is solved numerically within a computational domain shown in Fig. 4, where the boundary conditions for $\mathbf{u}$ and p are also provided. This computational domain stems from the boundary-value problem shown in Fig. 3(b), in which the lower boundary corresponds to the axis of symmetry. The length of the computational domain (in x direction) is chosen to be $10L$ and its height (in r direction) is $3L$. In free-swimming cases (Sec. IV C), to prevent the swimmer from moving out of the computational domain a uniform incoming flow u_0 is introduced (see Fig. 4). The value of u_0 is determined through numerical tests. The effect of this incoming flow is removed in post processing so that the results presented are measured in a space-fixed coordinate system without background flow. In tethered swimming cases (see Sec. IV B), the horizontal position of the swimmer is kept at the center of the domain and u_0 is set to be zero.

To discretize the partial differential equations, a finite-difference algorithm is developed, which combines a second-order method for spatial discretization and the Crank-Nicholson method (also

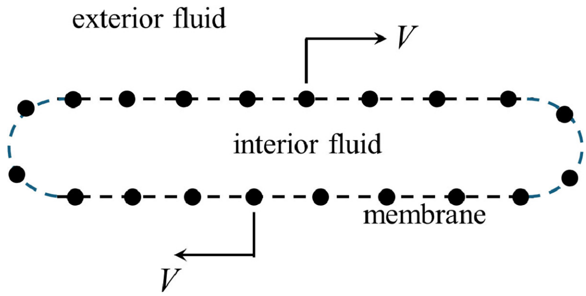

FIG. 5. Numerical rendition of the membrane circulation. The contour of the wall is shown in dashed line, and the numerical grids on the membrane are shown as bullets.

second order in accuracy) for time integration. The computational domain is separated into two regions, an inner region near the solid object where refined computational mesh is used for high resolution, and an outer region with coarser computational mesh for high efficiency in computation (Fig. 4). In the inner region the grid size is uniform; in the outer region the grid size increases gradually with the distance to the inner region. The transition from the inner mesh to the outer one is smooth. The details of this method can be found in previous publications [18–20].

Numerically, the circulation of the membrane is achieved in a manner illustrated in Fig. 5. In the immersed-boundary approach, the solid structure (hereby the membrane that separates the interior fluid from the exterior fluid) is represented by isolated grids embedded in the surrounding flow field. During the simulation these grids move along the contour of the wall (i.e., in the s direction) with the prescribed speed V. This brings the nearby fluid to move together according to the no-slip/no-flux conditions enforced via Eq. (3). The interior flow does not affect the net force F_b on the body, as the force it exerts on the membrane is an internal force. However, it does affect the power expenditure P through energy dissipation.

The accuracy of the numerical solver used in this study has been demonstrated by using it to simulate a canonical problem, the flow around a stationary sphere [19]. The results matched well with benchmark data from the literature. Moreover, numerical sensitivity tests have been conducted with various configurations [19,21].

An additional validation of the current model is carried out by examining the drag force caused by flow around a fixed torus. As shown in Fig. 6, the torus has a major radius of $D/2$ and a minor radius of $d/2$ so that its aspect ratio is D/d. The Reynolds number R_e is defined by using the incoming flow speed U and d. Numerically, the size of the computational mesh is $\Delta x = \Delta r = 0.005d$, the time step is $1 \times 10^{-4} d/U$, and the computational domain is $20d \times 10d$.

In Fig. 7 the drag coefficient C_D (defined as $F_D/(\frac{1}{2}\pi \rho D d U^2)$, where F_D is the drag force on the torus) at various Reynolds numbers when $D/d = 2$ is plotted. The predictions of our model are compared with the numerical results reported by Sheard *et al.* [22]. It is seen that the two sets of data agree perfectly with each other.

IV. RESULTS

To normalize the problem, We choose the fluid density ρ, the membrane circulation speed V, and the body length L as repeating variables. Thus, in the following results the lengths are normalized by L, the speeds by V, the time by $V^{-1}L$, the masses by ρL^3, the forces by $\rho L^2 V^2$, the power by $\rho L^2 V^3$, and the vorticity by $L^{-1}V$. For convenience, we do not change the symbols of the variables defined earlier, although hereafter they are all dimensionless.

In the following simulations the body mass m_b is chosen to be 0.005. This parameter does not affect the steady-state performance of the system, although it does affect the route toward steady state. The wall thickness d is fixed at 0.08. The physical parameters that can be changed are: (1) the

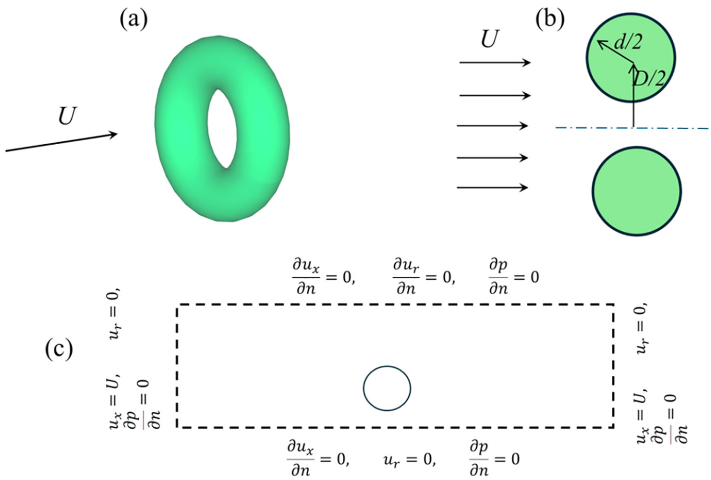

FIG. 6. (a) Three-dimensional illustration of flow around a fixed ring. (b) Two-dimensional view of the problem in a cross section. (c) Computational domain.

Reynolds number, which is changed by varying μ, and (2) the diameter of the body D. The range of R_e considered in this study is [10, 400]. Above this range, the axisymmetric assumption may be invalid at larger Reynolds numbers. Below this range, the power expenditure increases dramatically so that the efficiency decays.

A. Numerical sensitivity tests

To further examine the validity and accuracy of the numerical model in the current study, and to choose the proper numerical parameters, additional sensitivity tests have been conducted. For this purpose we study three different meshes, a coarse mesh with $\Delta x = \Delta r = 0.0045$ and $N_s = 667$, a

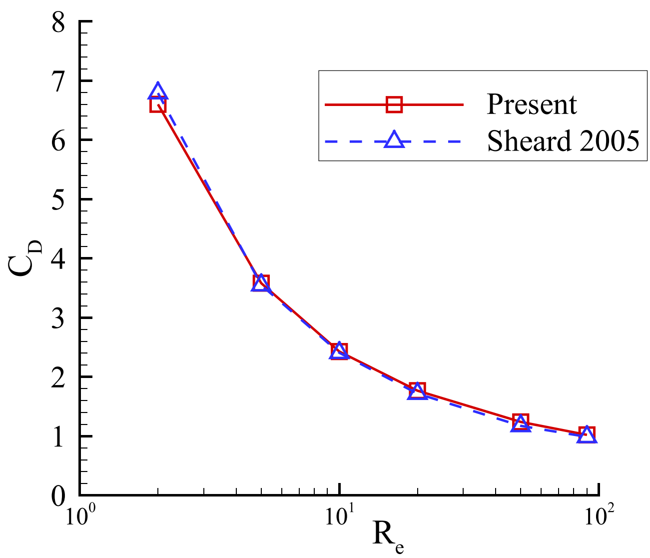

FIG. 7. Drag coefficient on a torus with an aspect ratio of $D/d = 2$ at different Reynolds numbers obtained with the present method in comparison with the results reported by Sheard *et al.* [22].

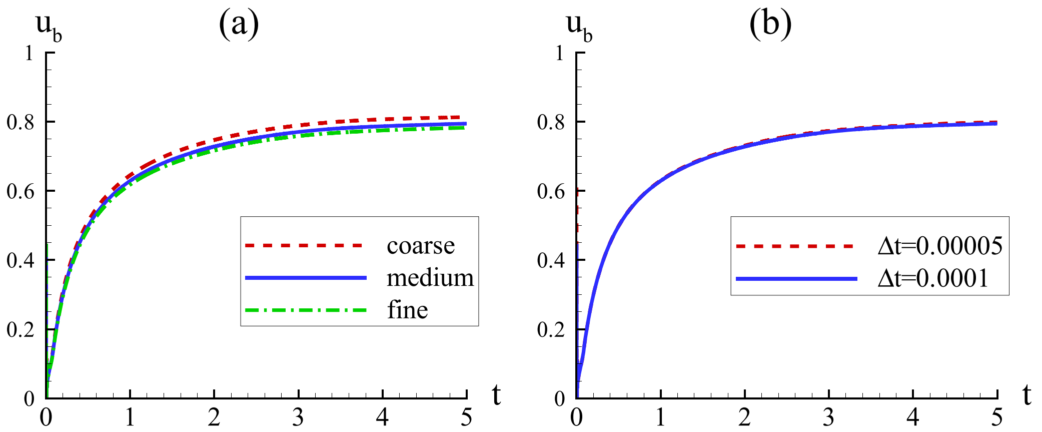

FIG. 8. Sensitivity of the time history of the swimming speed u_b to (a) computational mesh and (b) time step. $\mathrm{R_e} = 40$, $D = 0.3$.

medium one with $\Delta x = \Delta r = 0.003$ and $N_s = 1000$, and a fine one with $\Delta x = \Delta r = 0.002$ and $N_s = 1500$. Here Δx and Δr are the sizes of the computational grid in x and r directions in the inner region. N_s is the number of grids along the membrane. Two values of time step, $\Delta t = 5 \times 10^{-5}$ and $\Delta t = 10^{-4}$, are also tested. In Fig. 8, it is demonstrated that the numerical results (represented by the time history of the swimming speed $u_b = \dot{x}_b$) are not sensitive to these numerical parameters.

In addition, sensitivity to the size of the computational domain has been tested by using a domain that is 1.5 times larger than the one described in Sec. III B in each side. The mesh size in the inner region remains unchanged. It is shown that this change in the numerical setup has almost no effect on the result. The figure is not displayed here as the two curves with the smaller and larger domains are graphically indistinguishable from each other.

All the following simulations will be conducted with the medium mesh, a time step of 10^{-4}, and a computational domain specified in Sec. III B.

B. Tethered mode

In the tethered mode the forward motion x_b is set to be zero. The purpose is to examine the force generation capacity of the system at different conditions, i.e., different values of $\mathrm{R_e}$ and D. Usually the membrane has to circulate around for about two to five times before steady state is established. Afterwards the net force F_b, the power expenditure P, and the near-body flow field are recorded.

The near-body flow field in the steady state for a typical case with $\mathrm{R_e} = 200$ and $D = 0.3$ is shown in Fig. 9. According to Fig. 9(a), inside the chamber the longitudinal component of the flow velocity u_x is close to the speed of the inner-side membrane (i.e., -1), whereas the flow speed in the outer side drops quickly as the distance to the outer surface increases. Meanwhile, the radial velocity component u_r is small except in the areas close to the leading and trailing edges of the wall.

In addition, contour of the vorticity component $(\partial u_x/\partial r - \partial u_r/\partial x)$ is plotted in Fig. 9(c). It is seen that the magnitude of the vorticity inside the chamber is small, which is consistent with the fact that the variation of the flow velocity in the chamber is small [see Figs. 9(a) and 9(b)]. However, near the outer side of the wall there is an area with concentration of negative vorticity, indicating the shear flow induced by the tangential speed of the wall due to the membrane circulation. The difference in the strength of the vorticity fields near the inner side and the outer side of the wall implies that the shear strengths, and subsequently the shear stresses, in these two regions are different.

Areas in a flow field with concentrated vorticity often coincides with the existence of vortices. With our definition, concentration of positive vorticity corresponds to a clockwise vortex while concentration of negative vorticity corresponds to a counterclockwise vortex. To check the existence

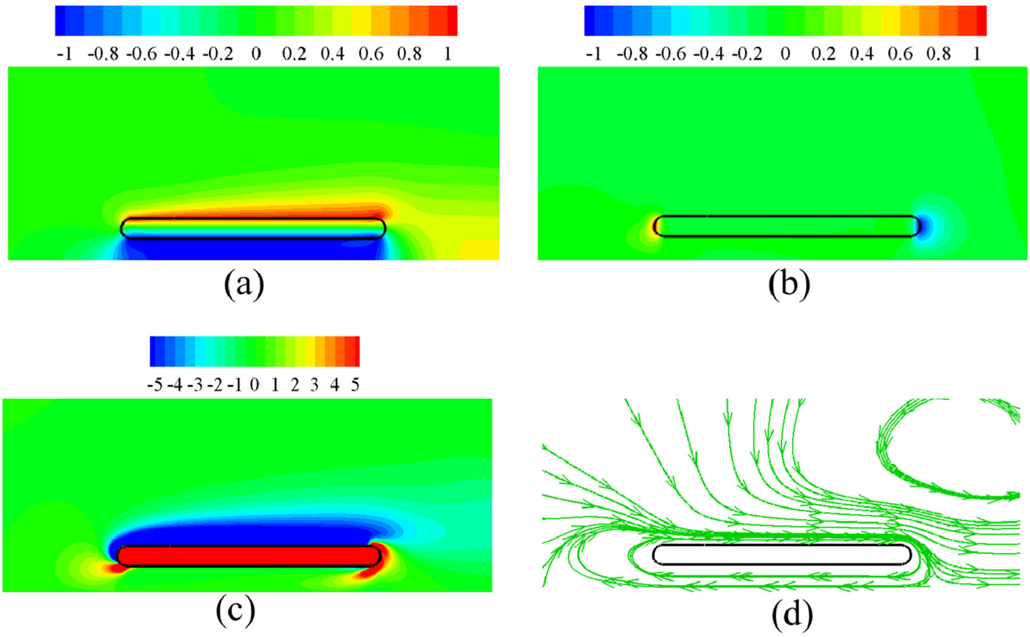

FIG. 9. Near-body flow field around a tethered swimmer visualized through (a) contour of u_x, (b) contour of u_r, (c) contour of vorticity, and (d) streamlines. $\mathrm{R_e} = 200$, $D = 0.3$.

of vortices in the flow field, in Fig. 9(d) the streamlines near the swimmer are plotted. This figure suggests that the area with concentrated negative vorticity in Fig. 9(c) is not a vortex. Instead, there does exist a counterclockwise vortex slightly downstream. However, this vortex appears to be weak so that it is not detectable in the vorticity contour.

In the case shown in Fig. 9, the force F_o generated by the outer-side membrane (defined as the part of the membrane whose r position is larger than $D/2$), is 0.2. Meanwhile, the inner-side membrane (the part of the membrane whose r position is less than $D/2$) generates a negative force $F_i = -0.141$. Similar to the net force F_b, the positive direction of both F_o and F_i is the swimming direction $-x$. The difference between the magnitudes of F_o and F_i is attributed to the effect of the solid boundary. The inner-side membrane is located within a semiclosed chamber, in which it interacts with the wall on the opposite side of the chamber hydrodynamically, leading to a ground-effect-like phenomenon [21]. The outer-side membrane, however, is located within a semiopen field. This difference leads to the inner side versus outer-side asymmetry, which is essential for thrust generation. In this particular case, the net force generation is $F_b = F_o + F_i = 0.059$. The power expenditure P is 0.398.

The flow fields, visualized through streamlines, at various values of the Reynolds number $\mathrm{R_e}$ and body diameter D are shown in Fig. 10. Two values of $\mathrm{R_e}$ (10 and 200) and three values of D (0.3, 0.4, and 0.5) are included. These figures suggest that except for some local circulatory motions (e.g., the motion around the wall and the vortex downstream), the induced flow field is predominantly in the $+x$ direction. This kind of flow is expected to be associated with a net force on the body in the $-x$ direction. The Reynolds number has pronounced effect on the flow field—according to the streamline plots in all values of D the downstream vortex disappears when $\mathrm{R_e}$ is reduced from 200 to 10. As D increases, the region surrounding the wall within which the fluid circulates around it is enlarged.

For a clearer comparison among cases with different values of $\mathrm{R_e}$ and D, in Fig. 11 we plot profiles of the longitudinal velocity component u_x at a cross section downstream. These figures prove that with larger D the flow region affected by the motion of the wall increases in size. Besides,

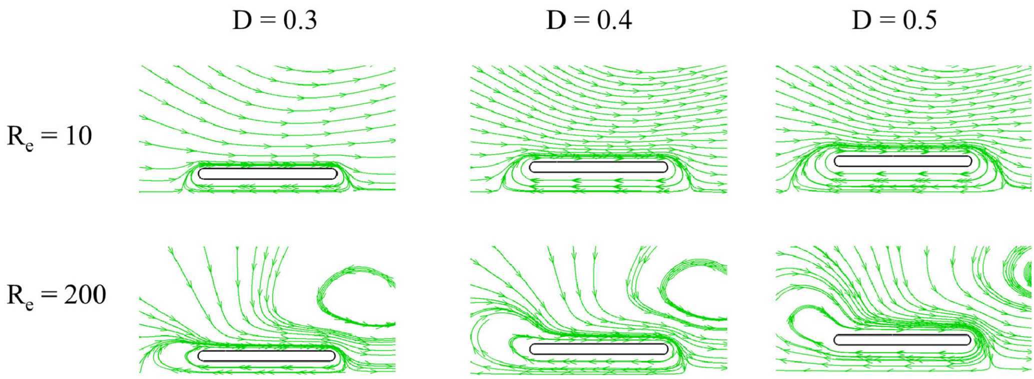

FIG. 10. Near-body flow field visualized through streamlines at $\mathrm{R_e} = 10$, 200 and $D = 0.3$, 0.4, and 0.5.

the area of the affected region is also larger for cases with low Reynolds number, a phenomenon attributed to the increased shear stress with higher viscosity.

Corresponding to the enlargement of the affected area in the flow field, lower Reynolds number also leads to the generation of larger net force, as demonstrated in Fig. 12(a). However, this enhancement of F_b is achieved at the cost of more energy spent to circulate the membrane [Fig. 12(b)].

The effect of diameter D on force generation is more complicated. On the one hand, larger D leads to more surface area of the membrane so that both F_o and F_i are increased. This effect tends to increase F_b. On the other hand, with larger D the effect of the solid boundary in the chamber is reduced so that the inner side versus outer-side asymmetry of the membrane is weakened. Subsequently the magnitudes of F_o and F_i are closer to each other. This effect tends to reduce F_b. The exact effect of D on F_b is therefore case dependent. In the lower Reynolds number regime ($\mathrm{R_e} <\sim 50$) the first effect triumphs over the second effect so that higher F_b is achieved at higher D. Beyond this Reynolds number regime the opposite trend is observed [see Fig. 12(a)]. In terms of the power expenditure, the trend is much simpler: larger D always increases P within the whole range of $\mathrm{R_e}$ we consider [Fig. 12(b)].

C. Free-swimming mode

In the free-swimming scenario the swimmer starts from rest ($u_0 = 0$), where the outer-side membrane generates positive force with respect to the swimming direction ($F_o > 0$) and the inner-side membrane generates negative force ($F_i < 0$). Propelled by the net force $F_o + F_i$, it accelerates toward

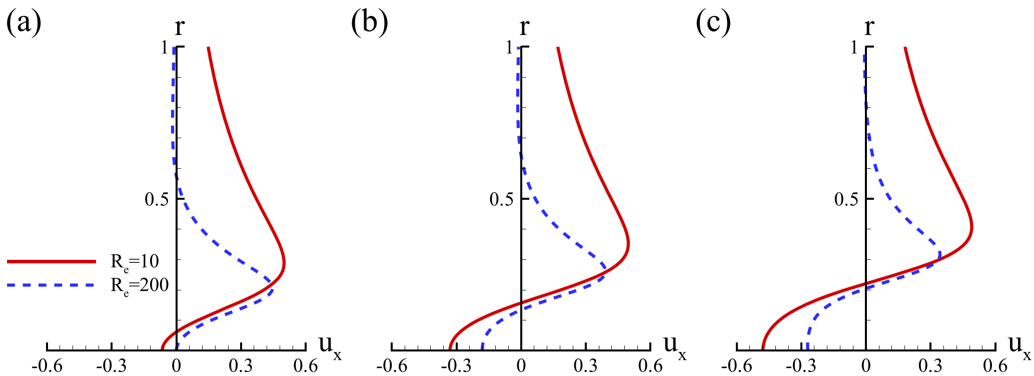

FIG. 11. Profiles of u_x at two values of $\mathrm{R_e}$ (10 and 200) and (a) $D = 0.3$, (b) $D = 0.4$, and (c) $D = 0.5$. The measurements are conducted at a distance of 0.1 downstream of the trailing edge of the swimmer.

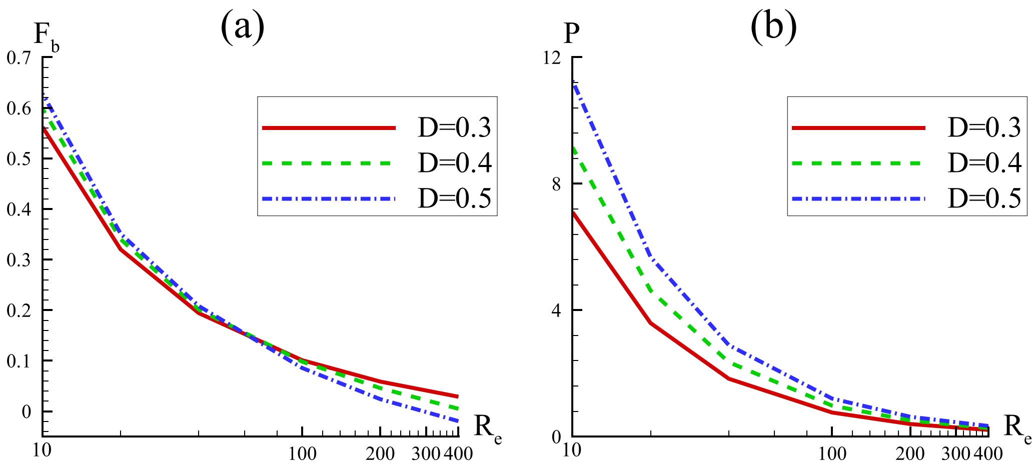

FIG. 12. (a) Net force F_b and (b) power expenditure P in steady state at different values of $\mathrm{R_e}$ and D in the tethered mode.

the $-x$ direction. As the forward speed u_b increases, the magnitude of F_o is reduced following the diminished relative motion between the outer-side membrane and the background flow. Meanwhile, the magnitude of F_i is increased since the relative motion between the inner-side membrane and the background flow is enhanced. The acceleration phase stops at the state when $F_o = -F_i$. Afterwards the swimmer travels at its steady-state swimming speed u_{bs}.

The dependencies of F_o and F_i upon u_b at two different Reynolds numbers are plotted in Fig. 13. Interestingly, despite the large differences in the exact values of F_o and F_i in these two cases, the steady-state swimming speeds are close to each other.

An intuitive explanation for the insensitivity of u_b to $\mathrm{R_e}$ is provided in the following. By invoking the Blasius solution, the shear force exerted by a flow on the surface of a flat plate aligned with it is approximated as $\alpha U^{3/2}\mu^{1/2}$, where U is the relative speed between the flow and the plate and α depends on the density of the fluid and the surface area of the plate. If we assume that this relation can be roughly applied to the surfaces of the swimmer with some adjustments to the coefficient α to account for surface curvature and boundary effects, then the shear force exerted by the exterior flow on the outer surface of the swimmer (the surface where the outer-side membrane lies on) could be $\alpha_o(V - u_b)^{3/2}\mu^{1/2}$ and the one on the inner surface (the surface where the inner-side membrane lies on) could be $\alpha_i(V + u_b)^{3/2}\mu^{1/2}$. The steady state is reached when these two forces are balanced so that we have

$$\frac{u_{bs}}{V} = \frac{1 - \left(\frac{\alpha_i}{\alpha_o}\right)^{2/3}}{1 + \left(\frac{\alpha_i}{\alpha_o}\right)^{2/3}}. \tag{8}$$

It is seen that when V and the fluid density are fixed, u_{bs} does not depend on the viscosity μ. However, in our formulation the variation of the Reynolds number $\mathrm{R_e}$ is achieved by varying μ. This explains why the dependence of u_{bs} upon $\mathrm{R_e}$ is weak.

Incidentally, within certain range of Reynolds number, it might be possible to quantitatively solve this problem by using the analytical solution for axisymmetric boundary layers [23]. However, if the Reynolds number is too low, then the boundary layer approximation is not accurate. If it is too high, then the flow will not be axisymmetric anymore.

Systematic simulations have been conducted to document the performance of the system during free swimming characterized by the steady-state swimming speed u_{bs}, the steady-state power expenditure P_s, and the cost of transport $\mathrm{Cot} \equiv P_s/u_{bs}$.

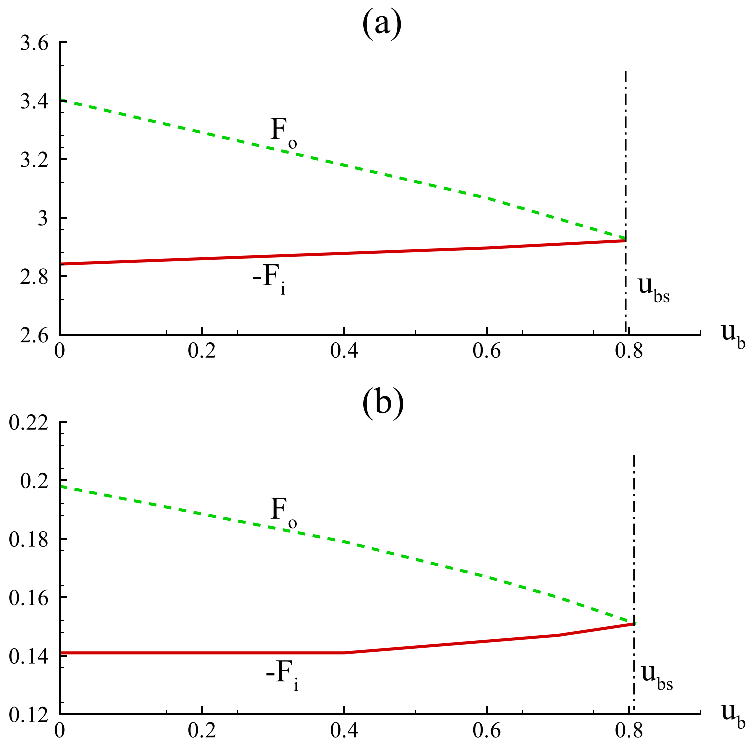

FIG. 13. Dependencies of the force generated by the outer-side membrane (F_o) and the one by the inner-side membrane (F_i) at different values of forward speed u_b with (a) $\mathrm{R_e} = 10$ and (b) $\mathrm{R_e} = 200$. $D = 0.3$.

Figure 14 demonstrates the performance of the swimmer at various combinations of $\mathrm{R_e}$ and D. It is seen that within its range considered in this study, the effect of $\mathrm{R_e}$ on u_b is rather small, which is consistent with the trend shown in Fig. 13. However, it does affect P—smaller $\mathrm{R_e}$ leads to higher P and subsequently higher CoT. However, as D is increased, u_b is reduced while P is increased. The combined effect is a pronounced increase of Cot with higher D within the whole range of $\mathrm{R_e}$ we consider.

Specifically, when D is 0.3, the swimming speed reaches 80% of the membrane circulation speed (in comparison, the maximum swimming speed of a toroidal swimmer is between 60% and 70% of the circulation speed [13,15]). When D is increased to 0.4, the speed drops to 70% of the circulation speed. In terms of CoT, the best performance with the range of parameters is achieved at $D = 0.3$ and $\mathrm{R_e} = 400$, where the values of CoT is around 0.21. Unfortunately, the energy expenditure of a toroidal swimmer at finite Reynolds numbers has not been reported so that it is not possible to compare the efficiencies of the two designs.

For a representative case, the near-body flow fields recorded in a body-fixed reference system are displayed in Fig. 15. Compared with the case shown in Fig. 9 (note that these two cases share the same $\mathrm{R_e}$ and D), there are a few differences:

(1) Outside of the barrel, there is a nonzero flow speed u_x away from the body in the longitudinal direction caused by the leftward motion of the swimmer [Fig. 15(a)]. However, inside the chamber there is little change in u_x.

(2) The vorticity strength above the outer-side membrane is greatly reduced [Fig. 15(c)]. This is attributed to the fact that the relative speed between the outer-side membrane and the flow near it is reduced.

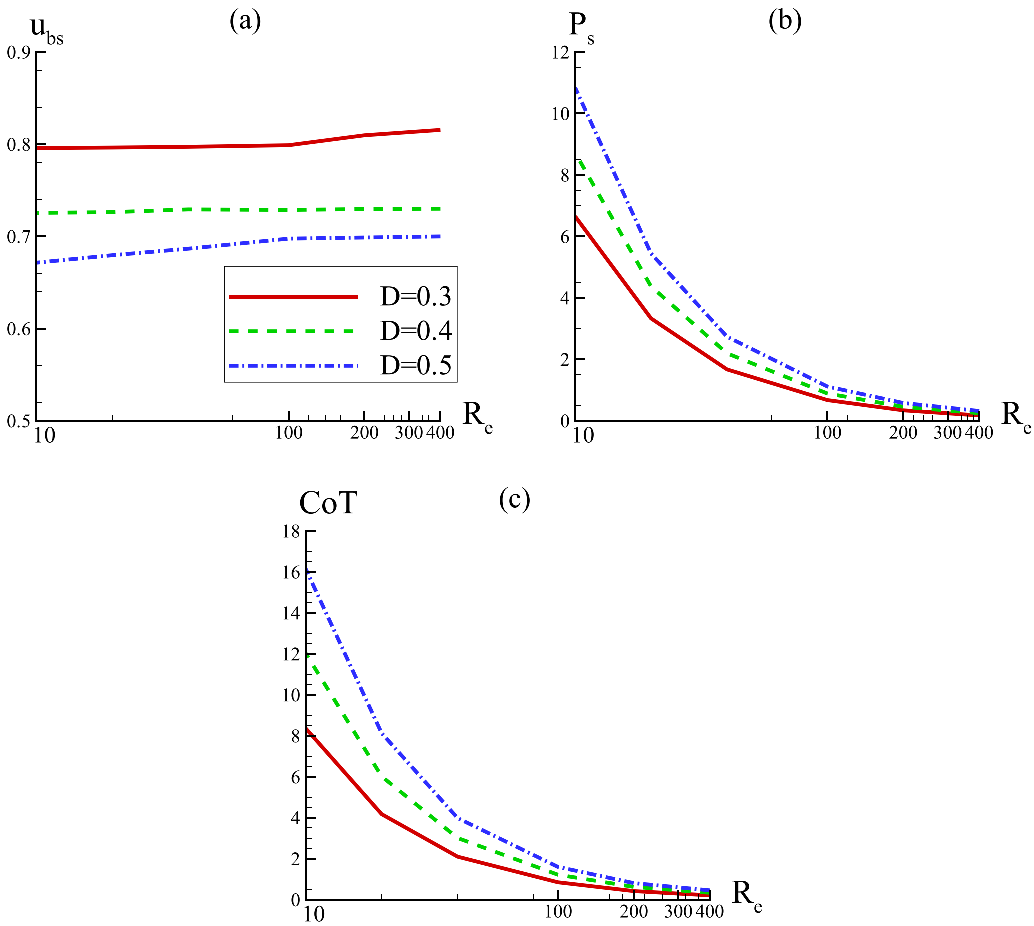

FIG. 14. (a) Swimming speed u_{bs}, (b) power expenditure P_s, and (c) CoT in steady state at different values of R_e and D in the free-swimming mode. The swimming direction is $-x$ (see Fig. 3).

(3) According to the streamlines, there is no vortex downstream [Fig. 15(d)]. This again can be explained by the reduced relative motion between the outer-side membrane and the flow near it so that the vorticity shed from the membrane into the wake is mitigated.

V. CONCLUSIONS

By using a numerical model based on the immersed-boundary method, we have computationally investigated the feasibility and potential performance of a swimmer relying on tank-treading motion of its membrane for thrust generation in the Reynolds number range of $O(10-10^2)$. The basic design includes a barrel-shaped body with both the front and the back ends open. Its side wall is made of a membrane with fluid inside. Both tethered and free-swimming modes have been examined.

In the tethered mode, our simulations indicate that positive net force (with respect to the swimming direction) is generated when the inner-side membrane travels upstream to create negative force while the outer-side membrane travels downstream to create positive force. During this process positive net force is achieved since the outer side of the membrane generates more force. This net force decreases when the Reynolds number is increased. The dependence on the body diameter D is more complicated. At lower Reynolds numbers, this force increases with larger D. However, at

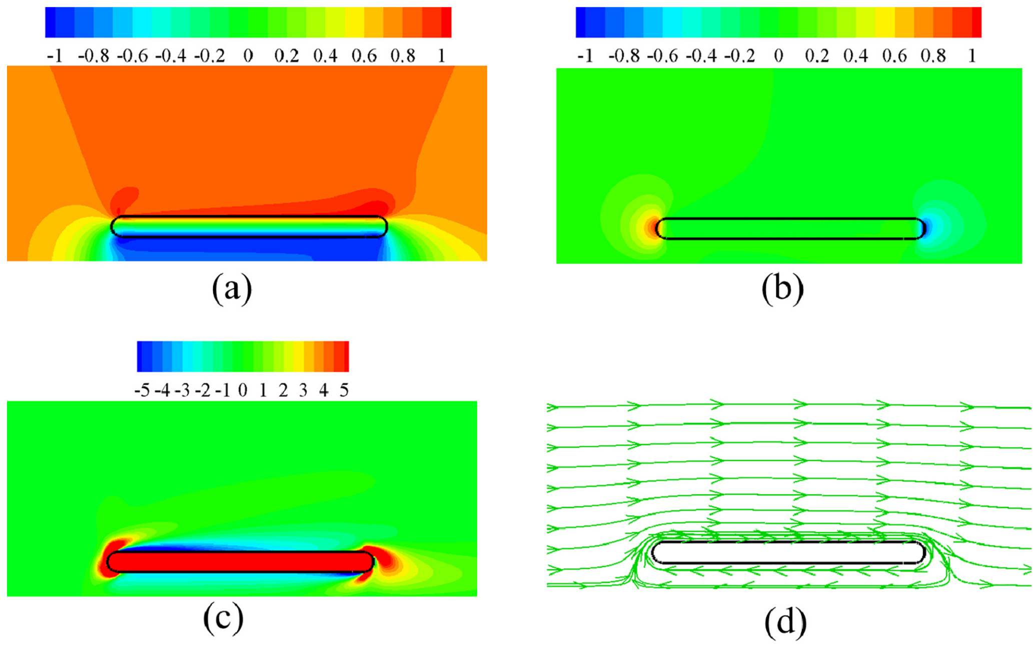

FIG. 15. Near-body flow field around a free-swimming swimmer visualized through (a) contour of u_x, (b) contour of u_r, (c) contour of vorticity, and (d) streamlines. $\mathrm{R_e} = 200$, $D = 0.3$. The flow field is recorded in a body-fixed coordinate system.

higher Reynolds numbers the trend is reversed. The power expenditure to activate the membrane decreases with $\mathrm{R_e}$, but it increases with D.

In the free-swimming mode, it is found that the forward speed at steady state drops when D is increased. It is, however, not sensitive to the Reynolds number. Consequently, the cost of transport is reduced at higher values of $\mathrm{R_e}$, suggesting that the swimmer works more efficiently in higher Reynolds number regime. Unfortunately due to the limitation of the numerical model it is not possible to go beyond the upper range of the Reynolds number (400) considered in this study. Future investigation in that study may be interesting. Besides, optimization studies about the geometric design of the system for better swimming speed or efficiency will be an interesting direction to go. Moreover, similar to the toroidal swimmer [16], the swimming direction of our design may be reversed at certain regions in the parametric space due to the jet-driven effect. More simulations are needed to explore this possibility.

As the current model is only capable of simulating objects with no thickness, we have focused on a design in which the wall of the swimmer is made of fluid enwraped within a thin and flexible membrane. The interior fluid has the same physical properties as the exterior fluid. In reality, there could be detailed structure within the wall that is not taken into account in our model. This simplification does not affect the net force on the body, as the force exerted on the membrane by the interior structure or fluid is a internal force. However, it may affect the energy expenditure of the system as it takes energy to drive the internal fluid (in an actual design there may not be interior fluid) so that both the power expenditure and the cost of transport may be over estimated. In future studies more sophisticated models are needed for more accurate investigation of the energetics.

In a more general sense, the swimming mode of microorganisms using synchronized motion of cilia bears certain similarity to the tank-treading-driven locomotion method. In fact, these swimming processes are often modeled as distributed surface velocities associated with ciliary motion (squirming) [24]. This swimming method, although more complicated than the tank-treading one, provides more freedom in surface velocity distribution so that it might be able to deliver higher performance.

Finally, we point out that if the axisymmetric swimmer proposed in this study is not easy to be manufactured with the existing technology, then simplified versions with similar underlying physics might be useful for a pilot study. For example, a pair of parallel circular cylinders that rotate in opposite directions share the same mechanism of force generation as the toroidal swimmer [17]. Experimental studies of this simple device in thrust generation might be an interesting topic.

DATA AVAILABILITY

The data that support the findings of this article are not publicly available. The data are available from the authors upon reasonable request.

[1] R. Blake, *Fish Locomotion* (Cambridge University Press, Cambridge, UK, 1983).

[2] G. Lauder, Caudal fin locomotion in ray-finned fishes: Historical and functional analyses, Am. Zool. **29**, 85 (1989).

[3] S. Vogel, *Life in Moving Fluids. The Physical Biology of Flow*, 2nd ed. (Princeton University Press, Princeton, NJ, 1994).

[4] G. Triantafyllou, M. Triantafyllou, and D. Yue, Hydrodynamics of fish swimming, Annu. Rev. Fluid Mech. **32**, 33 (2000).

[5] Q. Zhu and Q. Xiao, Physics and applications of squid-inspired jetting, Bioinspir. Biomim. **17**, 041001 (2022).

[6] T. Fischer, M. Stöhr-Liesen, and H. Schmid-Schönbein, The red cell as a fluid droplet: Tank tread-like motion of the human erythrocyte membrane in shear flow, Science **202**, 894 (1978).

[7] D. Barthès-Biesel, Motion of a spherical microcapsule freely suspended in a linear shear flow, J. Fluid Mech. **100**, 831 (1980).

[8] R. Tran-Son-Tay, A study of the tank-treading motion of red blood cells in shear flow, Ph.D. thesis, Washington University, St. Louis, MO, 1983.

[9] Z. Peng and Q. Zhu, Deformation of the erythrocyte cytoskeleton in tank treading motions, Soft Matter **9**, 7617 (2013).

[10] P. Olla, Tank-treading as a means of propulsion in viscous shear flows, J. Fluid Mech. **680**, 265 (2011).

[11] E. Purcell, Life at low Reynolds number, Am. J. Phys. **45**, 3 (1977).

[12] R. Thaokar, H. Schiessel, and I. Kulic, Hydrodynamics of a rotating torus, Eur. Phys. J. B **60**, 325 (2007).

[13] A. Leshansky and O. Kenneth, Surface tank treading: Propulsion of Purcell's toroidal swimmer, Phys. Fluids **20**, 063104 (2008).

[14] Z. Deng, K. Li, A. Priimagi, and H. Zeng, Light-steerable locomotion using zero-elastic-energy modes, Nat. Mater. **23**, 1728 (2024).

[15] N. Moshkin and P. Suwannsri, Self-propelled motion of a torus rotating about its centerline in a viscous incompressible fluid, Phys. Fluids **22**, 113602 (2010).

[16] N. Moshkin and P. Suwannsri, Two regimes of self-propelled motion of a torus rotating about its centerline in a viscous incompressible fluid at intermediate Reynolds numbers, Phys. Fluids **24**, 053603 (2012).

[17] W. van Rees, G. Novati, and P. Koumoutsakos, Self-propulsion of a counter-rotating cylinder pair in a viscous fluid, Phys. Fluids **27**, 063102 (2015).

[18] K. Kim, S. Baek, and H. Sung, An implicit velocity decoupling procedure for the incompressible Navier–Stokes equations, Int. J. Numer. Meth. Fluids **38**, 125 (2002).

[19] X. Bi and Q. Zhu, Pulsed-jet propulsion via shape deformation of an axisymmetric swimmer, Phys. Fluids **32**, 081902 (2020).

[20] X. Bi and Q. Zhu, Free swimming of a squid-inspired axisymmetric system through jet propulsion, Bioinspir. Biomim. **16**, 066023 (2021).

[21] Q. Zhu, Dynamics of a wavy axisymmetric swimmer, AIAA J. **61**, 3598 (2023).
[22] G. Sheard, K. Houriga, and M. Thompson, Computations of the drag coefficients for low-Reynolds-number flow past rings, J. Fluid Mech. **526**, 257 (1999).
[23] P. Kumar and K. Mahesh, Analysis of axisymmetric boundary layers, J. Fluid Mech. **849**, 927 (2018).
[24] O. Pak and E. Lauga, Generalized squirming motion of a sphere, J. Eng. Math. **88**, 1 (2014).